Effect of the odd and even number of blades on the hydrodynamic performance of a pre-swirl pumpjet propulsor EP

Denghui Qin (秦登辉),[1,2] (iD) Qiaogao Huang (黄桥高),[1,2,a] (iD) Guang Pan (潘光),[1,2] Liming Chao (朝黎明),[1,2]
Yang Luo (罗扬),[3] (iD) and Peng Han (韩鹏)[4] (iD)

AFFILIATIONS

[1] School of Marine Science and Technology, Northwestern Polytechnical University, Xi'an 710072, China
[2] Key Laboratory for Unmanned Underwater Vehicle, Northwestern Polytechnical University, Xi'an 710072, China
[3] Department of Naval Architecture, Ocean and Marine Engineering, University of Strathclyde, Glasgow G4 0LZ, United Kingdom
[4] LadHyX, Department of Mechanics, CNRS, Ecole Polytechnique, 91128 Palaiseau, France

[a] Author to whom correspondence should be addressed: huangqiaogao@nwpu.edu.cn

ABSTRACT

A numerical study based on detached eddy simulations is conducted to investigate the effects of the odd and even number of rotor/stator blades, that is, on n_r/n_s, on the hydrodynamic performance of a pre-swirl pumpjet propulsor (PJP). In this paper, six PJPs, the PJP 6-4 (n_s–n_r), 8-6, 10-8, 7-5, 9-7, and 11-9, are created. The hydrodynamic performance, the unsteady force of blades, and the wake structure of the PJPs are compared. The results show that the frequency of the fluctuating force of the whole rotor highly depends on the number or, more specifically, the parity of n_r. When the parameter n_r is the even number, it can be found that the total unsteady force of the rotor blades will be strengthened at the k-order stator-blades-passing frequency ($k = 1/2n_r$). Moreover, it indicates that the superposition-enhancement coefficient (is defined as A^*) at $k = 1/2n_r$ equals to n_r, at least from the present tests. In terms of both the rotor and stator numbers are even, a phenomenon of the rotor–stator resonance occurs at $f = 1/2n_s n_r f_n$, where f_n represents the hub rotational frequency. This work is expected to give some insight in the design of a PJP.

Published under an exclusive license by AIP Publishing. https://doi.org/10.1063/5.0080661

I. INTRODUCTION

Pumpjet propeller (PJP) is a new type of propeller developed in recent years. It comprises a rotor (a rotating vane system), a stator (a stationary vane system), and a duct. According to the relative position of the stator and rotor, the PJP can be divided into two categories: the "pre-swirl PJP" (the stator is in front of the rotor) and the "post-swirl PJP" (the stator is behind the rotor).[1]

In this study, the hydrodynamic performance of a pre-swirl PJP is studied. For the pre-swirl PJP, the front stator can pre-swirl the incoming flow to improve the working conditions of the rotor. Hence, the propulsion efficiency of the rotor is improved. In addition, the front stator reduces the inlet flow of the rotor, leading to a reduction of the radiated noise of the PJP.[1] Therefore, since the birth of the PJP, it has received extensive attention, and research of PJP has grown rapidly.[2]

The experimental test is an essential means to study the flow-field characteristics of PJP. In 1963, McCormick and Elsenhuth[3] pointed out that PJP has apparent advantages in efficiency and

cavitation performance with respect to other traditional propellers through experimental data analysis. Subsequently, Hughes and Kinnas[4] proposed a ducted propeller with a pre-swirl stator [the front stator is nine-bladed, while the rotor is a modified four-bladed Massachusetts Institute of Technology (MIT) propeller]. This duct propeller was later known as the pre-swirl PJP. The hydrodynamic data of this model under different stator installation angles are tested in the water tunnel of the MIT. In addition, Suryanarayana et al.[5–7] have done a lot of research and experiments on a post-swirl PJP (with a 21-bladed stator and 15-bladed rotor). They have tested the hydrodynamic performance of PJP in the wind tunnel of the Indian Navy science and Technology Laboratory. Those experiments mainly focus on the thrust and torque of PJP under different working conditions.

Therefore, computational fluid dynamics (CFD) method is widely applied in the research of PJP due to the rapid growth of computing power.

Das *et al.*[8] conducted a numerical simulation of PJP (with a 21-bladed stator and 15-bladed rotor) based on standard $k - \varepsilon$ turbulence model, and the numerical results are in good agreement with the experimental results. Lu *et al.*[9,10] studied the hydrodynamic performance of PJP (with an 11-bladed stator and nine-bladed rotor) based on SST (the shear-stress transport) $k - \omega$ turbulence model. The formation, transportation, and development of rotor tip vortices are analyzed. Qin *et al.*[11] discussed the open water performance, pressure field, and velocity field of a PJP (with an 11-bladed stator and nine-bladed rotor) with different rotor tip clearances (0.2; 0.5; 1; 2, and 3 mm, respectively). The results show that with the increase in rotor tip clearance, the efficiency of the PJP gradually decreases. Qiu *et al.*[12] discussed the unsteady excitation force and pressure pulsation of a PJP (with an 11-bladed stator and nine-bladed rotor) under different oblique flow angles. Most of the aforementioned research works study the time average pressure/velocity field of PJP based on the Reynolds-averaged Navier–Stokes (RANS) equation combined with $k - \varepsilon$ or SST $k - \omega$ turbulence model.

In recent years, some researchers began to use detached eddy simulation (DES) or large eddy simulation (LES) method to study the unsteady flow field and the vortex structure of PJP. Sun *et al.*[13] simulated the flow of PJP (with a nine-bladed stator and seven-bladed rotor) using LES. Denghui *et al.*[1] discussed the difference of hydrodynamic performance between the pre-swirl PJP (with an eight-bladed stator and six-bladed rotor) and the post-swirl PJP (with an 11-bladed stator and nine-bladed rotor). The three-dimensional structure of vortices of rotor tip vortices of the two PJPs are compared. The vortex instabilities in the wake of the rotor of a pre-swirl PJP are studied based on the improved delayed detached eddy simulation (IDDES). The results show that the IDDES has well captured the generation and development of the tip vortices of PJP. A unique overlap–forward instability mode of the tip vortex is found.[14] Furthermore, the effect of the duct and the pre-swirl stator on the wake dynamics of a pre-swirl PJP (with an eight-bladed stator and six-bladed rotor) is numerically studied based on the IDDES.[2] In addition, the wake of this pre-swirl PJP and the vortex morphology is investigated using stress-blended eddy simulations.[15]

Until now, most of the research works are focused on the hydrodynamic performance and the wake dynamics of the pre-swirl pumpjet propulsor with a fixed number of blades, and less attention has been paid to the study of different rotor/stator blades numbers, especially the odd and even numbers. Few researchers studied the effect of blades number on the flow of the single or the ducted propeller. Felli *et al.* compared the flow of three E779A propellers with several different numbers of blades ($n = 2$, 3, and 4) in the water tunnel. The effect of the spiral-to-spiral distance on the wake instability of a single propeller is studied.[16] In addition, Gong *et al.* compared the vortex structures of six propellers (the single propeller with $n = 1$, 2, and 4 blades and the ducted propeller with $n = 1$, 2, and 4 blades). The tip vortex instability at the different number of blades is studied.[17] In addition, some of the research works are carried out to study the wake instability of a propeller,[18,19] a submarine,[20] and the wake–structure interaction between the propeller and rudder.[21–23] To the authors' best knowledge, the study of PJP with a different number of blades has not been carried out.

The PJP is always designed as an odd number of rotor/stator blades (such as 21, 15, 11, 9 stator blades and 15, 11, 9, 7 rotor blades) to avoid possible frequency resonance between rotor and stator.[2]

However, what are the conditions for the occurrence of resonance phenomenon? Is an even number of blades necessarily a poor solution? These problems still need to be further solved. The determination of the number of blades is usually one of the several parameters to be determined in the first step of PJP design. The choice of blade number also directly affects the hydrodynamic performance and the vibration performance of PJP. However, the direct comparison of the odd and even rotor/stator numbers on the flow of PJP has not been studied yet. An in-depth investigation of the underlying mechanisms of the flow of PJP with the odd and even rotor/stator number is worth for further investigation.

In the present work, the wake flow of a pre-swirl pumpjet propulsor with an odd and even rotor/stator number was investigated by numerical simulations. PJPs with 10/8/6 stator blades and 8/6/4 rotor blades and PJPs with 11/9/7 stator blades and 9/7/5 rotor blades are selected. The hydrodynamic performance, the unsteady force of blades, and the wake flow field of those PJPs are compared. This study aims to get insight into the relationships between the hydrodynamic performance and the parity of rotor/stator blades.

The paper is organized as follows. In Sec. II, the numerical methodology is discussed. Section III gives the numerical setup and the validations cases. Section IV studied the open water coefficient, the unsteady force of blades, and vortex structure of the PJP. Conclusions are finally given in Sec. V.

II. MATHEMATICAL AND NUMERICAL MODELS

The flow of PJP is simulated based on the Reynolds-averaged Navier–Stokes (RANS) equations

$$\frac{\partial u_i}{\partial x_i} = 0, \tag{1}$$

$$\frac{\partial (\rho u_i)}{\partial t} + \frac{\partial (\rho u_i u_j)}{\partial x_j} = -\frac{\partial p}{\partial x_i} + \frac{\partial}{\partial x_j}\left[\mu\left(\frac{\partial u_i}{\partial x_j} + \frac{\partial u_j}{\partial x_i}\right)\right]$$
$$+ \frac{\partial}{\partial x_j}(-\rho\overline{u'_i u'_j}) + S_j, \tag{2}$$

where x_i and x_j ($i, j = 1, 2, 3$) are the coordinate components, u_i and u_j are the corresponding velocity components, p is the pressure, ρ is the density of fluid, and μ is the dynamic viscosity. S_j is a generalized source term and $\rho\overline{u'_i u'_j}$ is the Reynolds stresses.

The improved delayed detached eddy simulation (IDDES) model[24] based on a modification of the shear stress transport (SST) $k - \omega$ model is used here,

$$\frac{\partial (\rho k)}{\partial t} + \nabla \cdot (\bar{\rho}\mathbf{U}k) = \nabla \cdot \left[\left(\mu + \frac{\mu_T}{\sigma_{k3}}\right)\nabla k\right] + P_k - \rho\beta^* k\omega F_{IDDES}, \tag{3}$$

$$\frac{\partial (\rho\omega)}{\partial t} + \nabla \cdot (\bar{\rho}\mathbf{U}\omega) = \nabla \cdot \left[\left(\mu + \frac{\mu_T}{\sigma_{k3}}\right)\nabla\omega\right] + (1 - F_1)2\rho$$
$$\times \frac{\nabla k \cdot \nabla\omega}{\sigma_{\omega 2}\omega} + \alpha_3\frac{\omega}{k}P_k - \beta_3\rho\omega^2, \tag{4}$$

$$F_{IDDES} = \frac{l_{RANS}}{l_{IDDES}}. \tag{5}$$

The complete formulation can be found in Ref. 25. Here, the equations are solved based on a commercial software (Ansys 16.0). For the DES approach studied here, the Pressure-Implicit with

Splitting of Operators (PISO) algorithm is used. A standard second-order scheme is used for the computation of Eulerian terms and viscous terms. In addition, the physical time is discretized by a bounded second-order method.

III. NUMERICAL SETUP

A. Model

In this paper, a pre-swirl pumpjet propulsor with eight stator blades ($n_s = 8$) and six rotor blades ($n_r = 6$) [see Fig. 1(a)] is selected, which is the same model in one of our numerical works before.[14] It is known that the blade numbers should not be an even number to avoid possible resonance between the rotor and the stator. To quantitatively evaluate the effect of the parity of n_r and n_s on the hydrodynamic performance of PJP, several new pre-swirl PJP models are created: the PJP 6-4 ($n_s = 6$, $n_r = 4$), 7-5 ($n_s = 7$, $n_r = 5$), 9-7 [$n_s = 9$, $n_r = 7$, see Fig. 1(b)], 10-8 ($n_s = 10$, $n_r = 8$), and 11-9 ($n_s = 11$, $n_r = 9$). An intuitive comparison of those models is shown in Figs. 1(c)–1(e). It can be seen that, for those PJPs, the hub and the duct (the maximum diameter of the duct is $D_d = 0.2200$ m) remain unchanged. In addition, one important thing that should be mentioned is that the change in the number of blades is not the replication of the original blades but to keep the disk ratio of the rotor and stator unchanged. The chord length and thickness of each section of the blade gradually change with the corresponding number of blades, while the pitch of each section remains unchanged. In addition, the central position of the rotor blade remains unchanged, and the axial position of the stator leading edge remains unchanged to keep the distance between the stator and

the hull unchanged. The comparisons of rotor and stator blades are shown in Fig. 1(f). The maximum diameter of the rotor is $D_r = 0.1664$ m.

A coordinate system of the PJP is established. The geometric center of the rotor is selected as the coordinate origin. The rotation axis is set as z-axis, and the x-axis is the vertically upward direction after assembly on the vehicle. The y-axis follows the right-hand rule.

B. Mesh details

The computational domain of the PJP models is the same, with a cylinder of diameter $10D_d$ and length $20D_d$. The inlet is $6D_d$ upstream of PJP as shown in Fig. 2. In addition, it can be seen that the computational domain is divided into four sub-domains: far-field domain, near-field domain, rotor domain, and stator domain. The near-field domain with diameter $1.5D_d$ and length $5D_d$ is selected to reduce the number of meshes using the strategy of the local grid refinement.[26]

For all the PJP models, the grid of the far-field domain and the near-field domain are the same as shown in Figs. 3(a) and 3(b), respectively. We can see several grid refinement areas: the wake region of the PJP model, the region behind the duct, the rotor blades tip region, and the wake region of the stator blades. In particular, the location and size of these grid refinement areas are determined according to the precalculated flow field results. Only when the mesh of the PJP is fine enough, the rotor–stator interaction can be accurately captured. In addition, the topology of rotor domain and stator domain of PJPs is the same. Considering the length of the paper, only the surface mesh

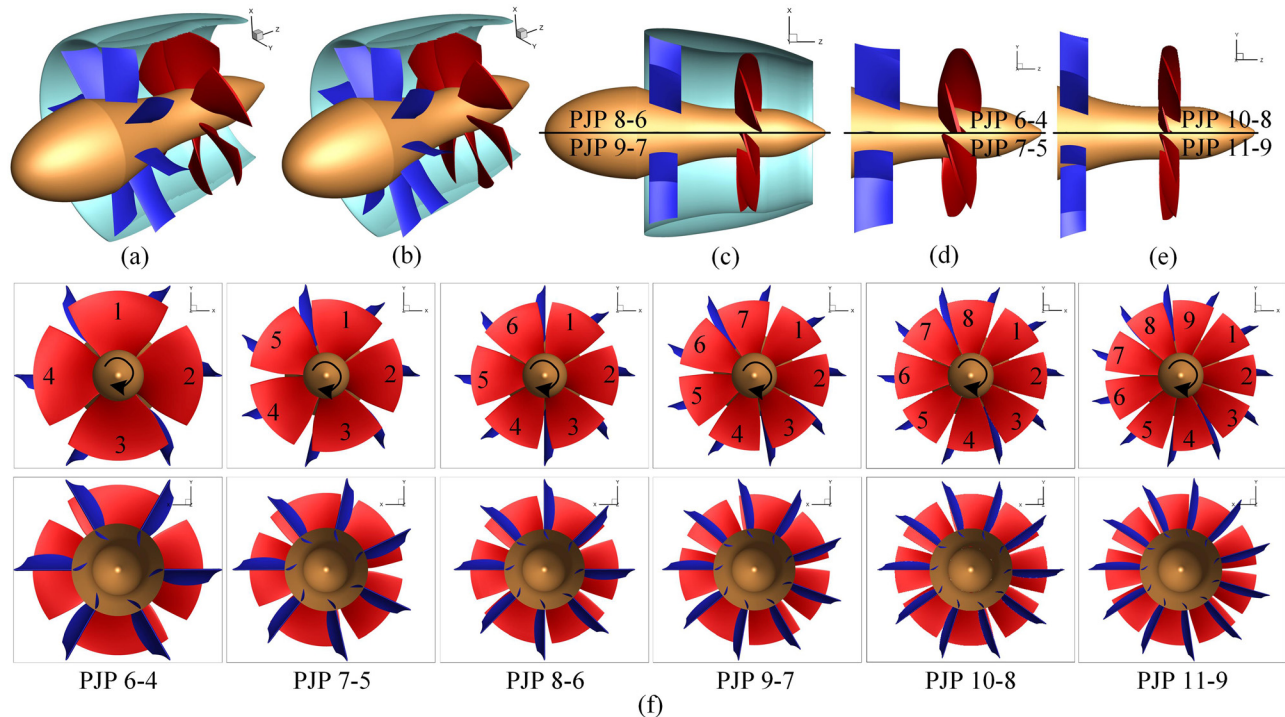

FIG. 1. The details of the PJP model: (a) the PJP 8-6 model; (b) the PJP 9-7 model; (c) side view of the PJP 8-6 and 9-7 model; (d) side view of the PJP 6-4 and 7-5 model; (e) side view of the PJP 10-8 and 11-9 model; and (f) the PJP models.
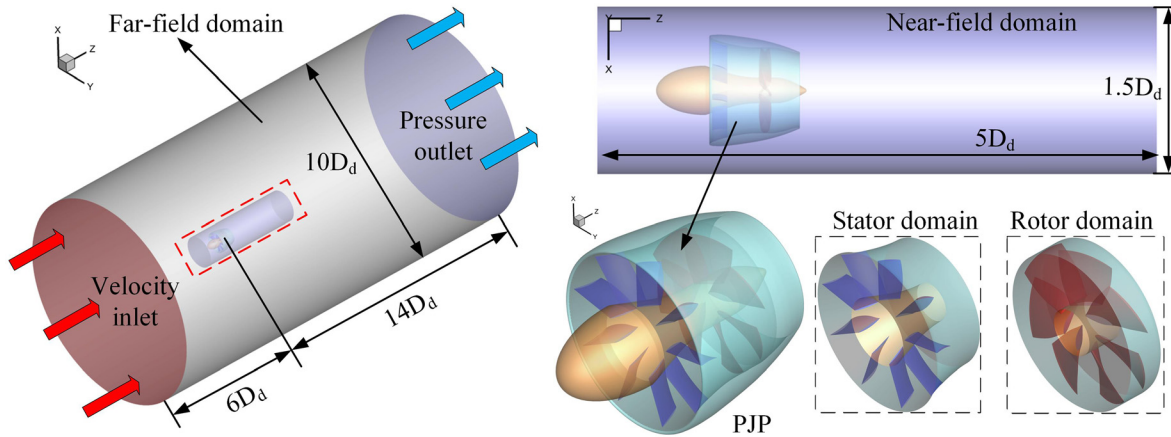
FIG. 2. Computational domains of the PJP 8-6 model.

of the PJP 8-6 and 9-7 is shown in Figs. 3(c) and 3(d), respectively. The same duct surface grid is illustrated in Fig. 3(e).

Table I lists the grid information for models. For the medium grid of the PJP 8-6 (as shown in Fig. 3), the mesh number of rotor domain, stator domain, near-field domain, and far-field domain is 10.53×10^6, 6.82×10^6, 11.44×10^6, and 1.52×10^6, respectively. The total mesh number of PJP 8-6 is 30.31×10^6, while that of the other PJP models is about $27.72 \times 10^6 \sim 36.09 \times 10^6$.

In addition, Fig. 2 shows the boundary condition setting. The inlet surface is using the velocity inlet boundary condition with U_0. The pressure outlet boundary with 0 Pa is applied to the outlet surface. The surfaces of the PJP are set as no-slip walls. In the simulation, the

rotational speed of the rotor domain is fixed as 1200 rev/min. The Reynolds number of PJP studied here is about $1.2 \times 10^5 - 8.5 \times 10^5$.

C. Validation and verification

To validate the numerical method, the simulation results are compared with the experiment of the PJP 8-6 model in the high-speed water tunnel of the Science and Technology on Water Jet Propulsion Laboratory, Marine Design and Research Institute of China. More details of the experimental data can be found in Ref. 14.

Table II lists the definitions of the nondimensional physical quantities used in the present study. In the table, n is the rotational
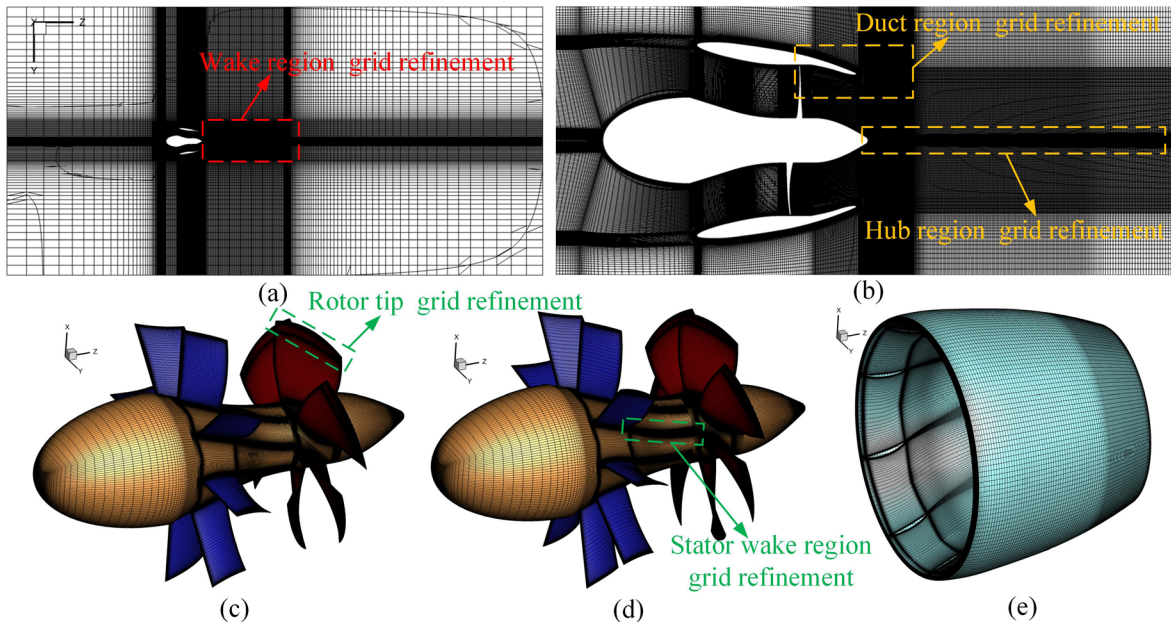

FIG. 3. Grid details of the PJPs: (a) the far field mesh; (b) the near field mesh; (c) the surface mesh of the PJP 8-6; (d) the surface mesh of the PJP 9-7; and (e) the duct surface mesh.

TABLE I. Grid information.

Working condition	Total number ($\times 10^6$)				
	Rotor domain	Stator domain	Near-field domain	Far-field domain	Total
PJP 8-6 coarse	4.32	4.29	3.20	0.72	12.53
PJP 8-6 medium	10.53	6.82	11.44	1.52	30.31
PJP 8-6 fine	20.14	11.93	20.54	2.05	54.66
PJP 6-4	8.16	6.60	11.44	1.52	27.72
PJP 7-5	8.95	7.20	11.44	1.52	29.11
PJP 9-7	12.08	7.54	11.44	1.52	32.58
PJP 10-8	12.89	8.69	11.44	1.52	34.54
PJP 11-9	14.08	9.05	11.44	1.52	36.09

speed of the rotor, which is fixed as $N = 1200$ rpm (rev/min, $n = 20$ rev/s) here. ρ equals to the fluid density, V is the far-field incoming flow velocity. T_r, T_s, and T_d are the thrusts of the rotor, stator, and duct, respectively. Q_r and Q_s are the torque of the rotor and the stator, respectively.

The predicted thrust coefficient of rotor, K_{Tr}, and torque coefficient of rotor, K_{Qr}, are compared with the experimental data in Fig. 4. As shown, the simulation results agree well with the experimental results, with a maximum relative error of about 4.48% (K_{Tr} at $J = 0.2$). In general, the DES approach used here can accurately predict the flow of PJP.

In addition, to carry out the grid independence test, a coarse grid and a fine grid are generated based on the medium grid of the PJP 8-6 model. The number of nodes decreases or increases, leading to a total mesh number of 12.53×10^6 for the coarse grid and 54.66×10^6 for the fine grid. The grid independence test has been discussed in detail

TABLE II. Nondimensional physical quantities.

| Physical quantity	Definition
Advance coefficient	$J = \dfrac{V}{nD_r}$
Thrust coefficient of rotor	$K_{Tr} = \dfrac{T_r}{\rho n^2 D_r^4}$
Torque coefficient of rotor	$K_{Qr} = \dfrac{Q_r}{\rho n^2 D_r^5}$
Torque coefficient of stator	$K_{Qs} = \dfrac{Q_s}{\rho n^2 D_r^5}$
Thrust coefficient of stator	$K_{Ts} = \dfrac{T_s}{\rho n^2 D_r^4}$
Thrust coefficient of duct	$K_{Td} = \dfrac{T_d}{\rho n^2 D_r^4}$
Total thrust coefficient	$K_T = K_{Tr} + K_{Ts} + K_{Td}$
Total torque coefficient	$K_Q = K_{Qr}$
Open water efficiency	$\eta = \dfrac{J}{2\pi} \dfrac{K_T}{K_Q}$
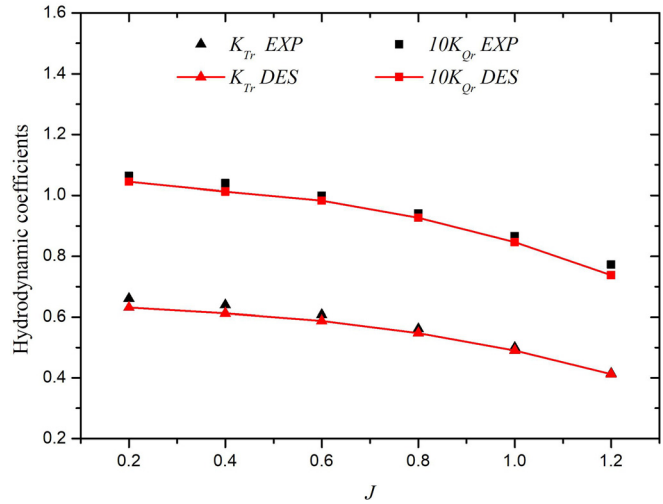
FIG. 4. Comparisons of IDDES simulations results with the experimental data.

in a previous article. Specific details of mesh refinement can be found in references.[26]

Based on the theory of Celik et al.,[27] the grid convergence analysis results are shown in Table III. The maximum error happens in the case $J = 0.4$ with only 0.98%. In general, the DES simulations results show good convergence with the refinement of the grid. Here, the medium-grid solution is adopted.

IV. RESULTS AND DISCUSSION
A. Hydrodynamic performance

For the convenience of later discussion, some variables are defined as follows: n_r is the number of rotor blades, n_s is the number of stator blades, n is the rotational speed of the rotor (in this research, it is fixed as $n = 20$ rev/s). $T_n = 0.05$ s is a hub rotation period, and the corresponding frequency is $f_n = 20$ Hz; $f_{BPF} = n_r f_n$ is the blades passing frequency of the rotor, and $f_S = n_s f_n$ is the blades passing frequency of the stator. In the frequency analysis of the unsteady variable, the frequency will be normalized as $k_1 = f / f_{BPF}$ and $k_2 = f / f_S$.

Figure 5 shows the comparison of the hydrodynamic performance of the PJP 8-6 and PJP 9-7. The hydrodynamic coefficient results of PJP are predicted based on the RANS simulation to save the calculation cost.

As shown in Fig. 5(a), the open-water efficiency of both PJP models, η, are nearly the same, only with a slightly decrease from 60.13% at $J = 0.9$ (for the PJP 8-6) to 59.71% at $J = 0.9$ (for the PJP 9-7). Hence, under the condition of keeping the disk ratio of blades

TABLE III. Grid convergence analysis.

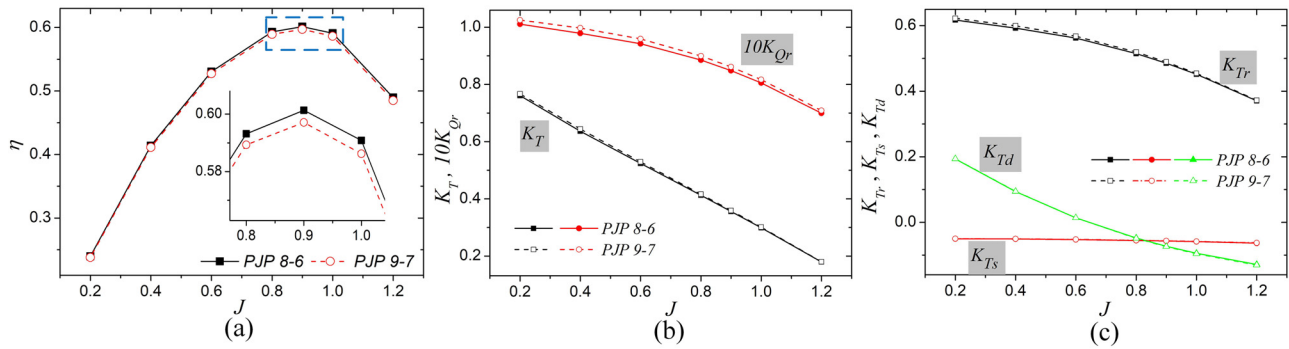| J	ϕ	Coarse	Medium	Fine	e_a^{32}	GCI_{medium}^{32}
0.4	K_{Tr}	0.6124	0.6121	0.6119	0.0003	0.28%
	K_{Qr}	0.1013	0.1017	0.1020	0.0029	0.98%
1.0	K_{Tr}	0.4903	0.4881	0.4873	0.0014	0.27%
	K_{Qr}	0.0847	0.0838	0.0843	0.0047	0.94%

FIG. 5. Hydrodynamic performance of PJPs: (a) the open water coefficient; (b) K_T and $10K_{Qr}$; and (c) K_{Tr}, K_{Ts} and K_{Td}.

unchanged, the number of blades has little effect on the open-water efficiency of the propeller.

As shown in Fig. 5(b), the K_T and $10K_{Qr}$ of the PJP 9-7 are slightly bigger than that of the PJP 8-6. Figure 5(c) compares the thrust coefficients of rotor (K_{Tr}), stator (K_{Ts}), and duct (K_{Td}) of PJPs. The results show that the K_{Tr} of PJP 9-7 is slightly larger than the PJP 8-6, while the K_{Ts} and K_{Td} are nearly the same. Hence, the difference of K_T for the two PJPs is mainly caused by the rotor. The increase in the number of blades has little effect on the thrust generated by the stator and duct.

Considering the length of the paper, the hydrodynamic coefficients of other models with different number of blades will not be

discussed here. Let us focus on the unsteady flow of those PJP models at different working conditions. The signals of unsteady thrust generated by the rotor/stator blades of the PJP are collected in a time range, which is equal to 14 periods of propeller revolution in the steady state (when the initial transient has completely died out).

For the PJP with even number of blades, at $J = 1.0$, the unsteady force of each rotor blade of the PJP 6-4, the PJP 8-6, and the PJP 10-8 is shown in Fig. 6. To quantitatively compare the rotor force of different PJP models, the unsteady force of each rotor blade is normalized to $K'_{Tr_i} = K_{Tr_i} - \overline{K_{Tr_i}}$ (the numbering sequence is clockwise viewing from the back of the model). As shown in the Figs. 6(a), 6(c), and 6(e), the unsteady force of each rotor blade, K_{Tr_i} ($i = 1, 2, 3, \dots$), of the
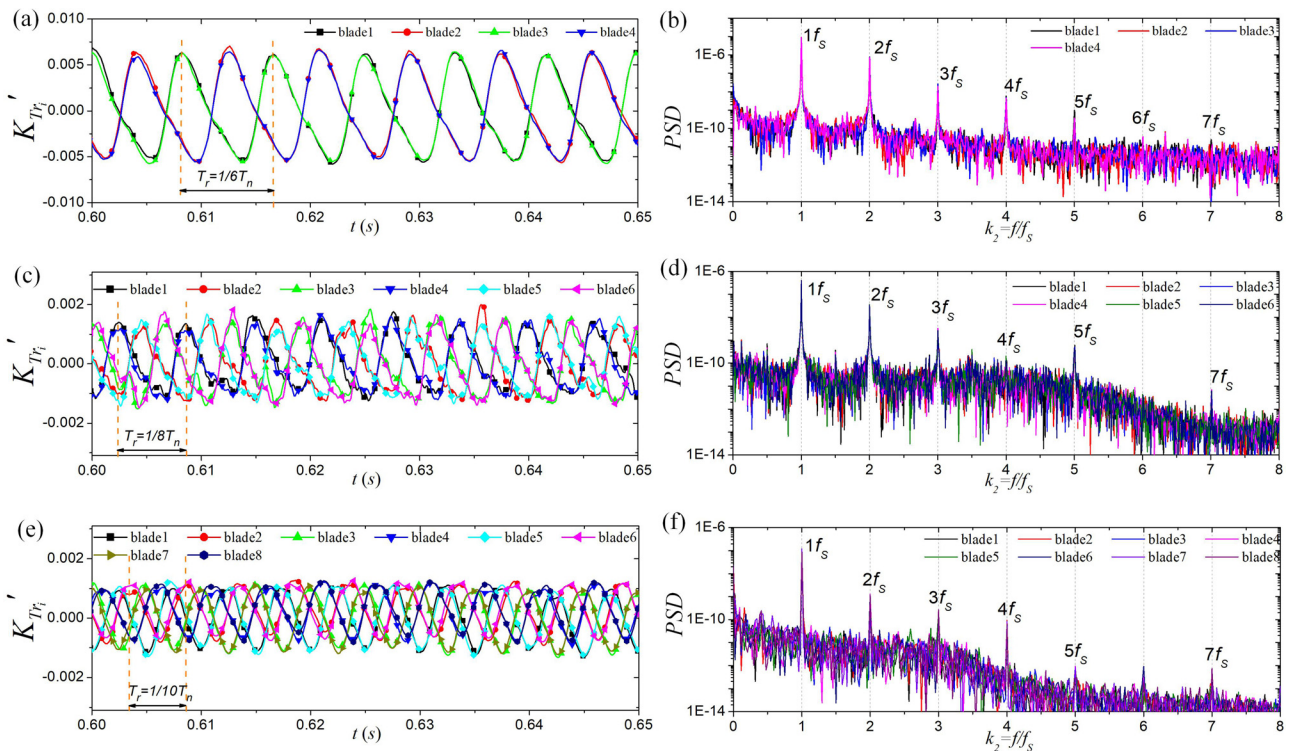

FIG. 6. The unsteady force of rotor blades in the case $J = 1.0$: (a) time history of the PJP 6-4; (b) PSD of the PJP 6-4; (c) time history of the PJP 8-6; (d) PSD of the PJP 8-6; (e) time history of the PJP 10-8; and (f) PSD of the PJP 10-8.

PJP 6-4, 8-6, and 10-8 is close to sinusoidal signals, and the variation period is $T_r = T_n/n_s$ ($T_n = 0.05$ s is a hub rotation period, and the corresponding frequency is $f_n = 20$ Hz).

The Fast Fourier Transform (FFT) analysis is carried out to study the frequency characteristics of the unsteady force. As shown in Figs. 6(b), 6(d), and 6(f), the power spectral density (PSD) spectrum of K_{Tr_i} of PJPs has the same peaks in nf_S (n = 1, 2, 3,..., and $f_S = n_s f_n$ is the stator blades passing frequency), which is consistent with the above periodic results.

Then, the force of the whole rotor (use $K'_{Tr} = K_{Tr} - \overline{K_{Tr}}$ here) of the PJP 6-4, the PJP 8-6, and the PJP 10-8 is shown in Figs. 7(a), 7(c), and 7(e), respectively. The PSD spectrum of the unsteady force of the rotor blade 1 (K_{Tr_1}) and the whole rotor (K_{Tr}) of the three PJPs is shown in Figs. 7(b), 7(d), and 7(f), respectively.

For the PJP 6-4, it can be seen that the total thrust of the rotor obtained by the superposition of the four rotor blades presents as a sinusoidal signal whose dominant frequency is $2f_S$. Compared with the PSD of K_{Tr_1}, the peaks at $1f_S$ and $3f_S$ disappear, replaced by a significant increase in the amplitude at $2f_S$.

For the PJP 8-6, the dominant frequency of PSD spectrum of the K_{Tr} is transferred from $1f_S$ to $3f_S$. Similarly, the dominant frequency of the PJP 10-8 is transferred from $1f_S$ to $4f_S$. Quantitatively, PSD amplitudes at $f = k_2 f_S$ ($k_2 = 1, 2, 3, \ldots n_r$) of K_{Tr_1} and K_{Tr} are compared as shown in Table IV. In the table, the 0.5 power of the amplitude ratio (PSD of K_{Tr}/PSD of K_{Tr_1}) is used due to that the amplitude of PSD is the square of the amplitude of FFT result.

The results show that, for a PJP with even number of rotor blades, the peaks at the k_2-order dominant frequency ($k_2 = 1/2n_r$) of the PSD of K_{Tr} is enhanced, while the peak amplitude at other orders changes little or even decreases significantly. As for the slightly increased amplitude, such as amplitude ratio $^{0.5}$ of 1.39 at $k_2 = 2$ and amplitude ratio $^{0.5}$ of 5.24 at $k_2 = 5$ for the PJP 10-8, it is due to that the amplitude of broadband component of PSD of K_{Tr} is obviously higher than that of K_{Tr_1} [see Fig. 6(f)].

In addition, it should be noted that the amplitude ratio $^{0.5}$ at $k_2 = 1/2n_r$ is just close to n_r. For the PJP 6-4, the amplitude enhancement coefficient of K_{Tr} is $3.86 \approx 4$ at $k_2 = 1/2n_r$, and it is $5.95 \approx 6$ for the PJP 8-6 and $7.85 \approx 8$ for the PJP 10-8. Therefore, it can be inferred that, for a PJP with even number of rotor blades n_r, a signal superposition enhancement phenomenon will happen at $k_2 = 1/2n_r$ with an amplitude enhancement coefficient of n_r.

To test this conjecture, a simple analysis of the superposition process of the unsteady forces of rotor blades is carried out. Here, we only discuss the FFT expansion results of the forces of a single blade and the whole rotor at $f = f_S$.

For a pre-swirl PJP with n_r rotor blades, at order $k_2 = 1$, the force of a single rotor blade can be simplified as

$$K_{Tri} = A_i \cos(2\pi f_S t - \varphi_i), \tag{6}$$

where the φ_i is the phase angle of the signal, and A_i is the corresponding amplitude calculated based on the FFT results of K_{Tr_i} ($i = 1, 2, 3, \ldots, n_r$).
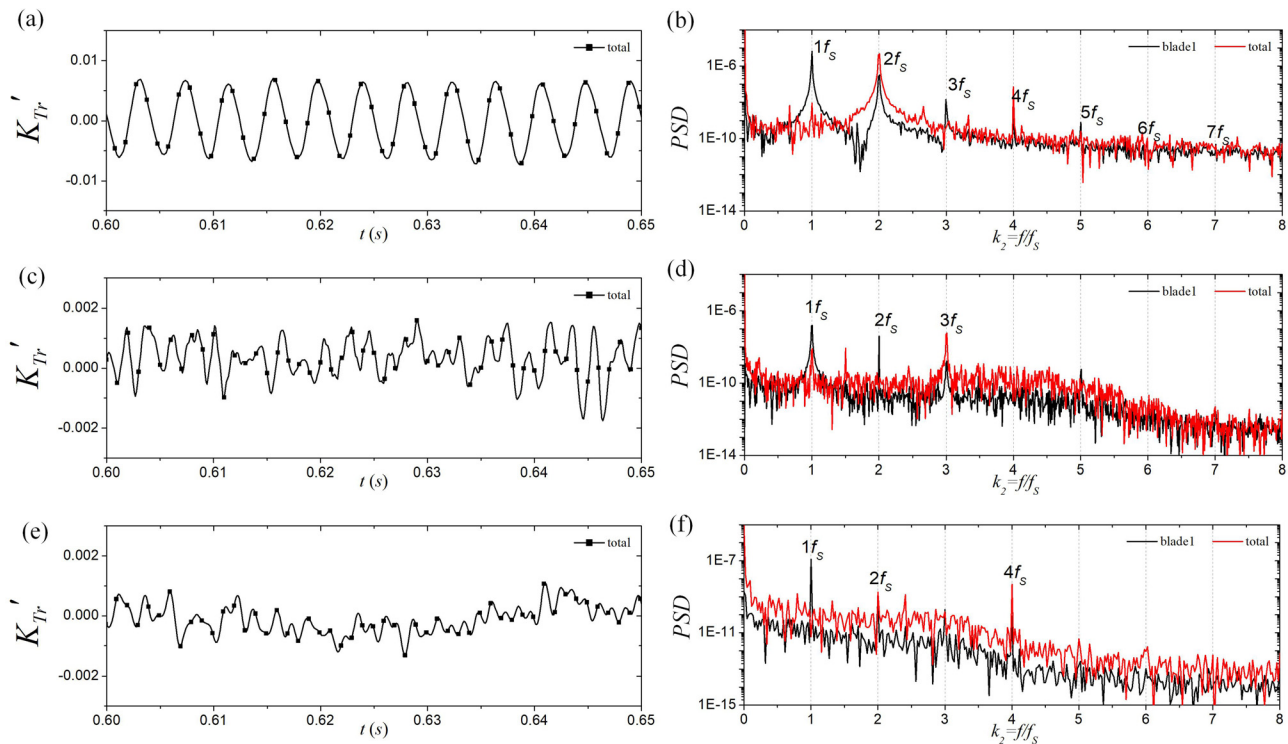

FIG. 7. The total unsteady force of rotor blades: (a) time history of the PJP 6-4; (b) PSD of the PJP 6-4; (c) time history of the PJP 8-6; (d) PSD of the PJP 8-6; (e) time history of the PJP 10-8; and (f) PSD of the PJP 10-8.

TABLE IV. Comparison of the PSD of the unsteady force between the single rotor blade and the total rotor.

Model	Thrust coefficient	$k_2 = 1$	$k_2 = 2$	$k_2 = 3$	$k_2 = 4$	$k_2 = 5$	$k_2 = 6$	$k_2 = 7$	$k_2 = 8$
PJP 6-4	K_{Tr_1}	6.48×10^{-6}	3.17×10^{-7}	1.39×10^{-8}	4.59×10^{-9}	$\cdots$	$\cdots$	$\cdots$	$\cdots$
	K_{Tr}	8.76×10^{-9}	4.73×10^{-6}	3.73×10^{-10}	6.90×10^{-8}	$\cdots$	$\cdots$	$\cdots$	$\cdots$
	Amplitude ratio $^{0.5}$	0.04	3.86	0.16	3.88	$\cdots$	$\cdots$	$\cdots$	$\cdots$
PJP 8-6	K_{Tr_1}	1.56×10^{-7}	3.95×10^{-8}	1.67×10^{-9}	3.10×10^{-10}	5.90×10^{-10}	8.22×10^{-12}	$\cdots$	$\cdots$
	K_{Tr}	7.91×10^{-9}	8.89×10^{-11}	5.92×10^{-8}	2.62×10^{-10}	3.74×10^{-11}	1.90×10^{-12}	$\cdots$	$\cdots$
	Amplitude ratio $^{0.5}$	0.23	0.05	5.95	0.92	0.25	0.48	$\cdots$	$\cdots$
PJP 10-8	K_{Tr_1}	1.20×10^{-7}	9.32×10^{-10}	1.95×10^{-10}	8.03×10^{-11}	1.63×10^{-13}	1.06×10^{-13}	1.11×10^{-14}	1.96×10^{-13}
	K_{Tr}	6.00×10^{-12}	1.80×10^{-9}	1.46×10^{-10}	4.94×10^{-9}	4.47×10^{-12}	9.27×10^{-13}	5.78×10^{-13}	7.28×10^{-13}
	Amplitude ratio $^{0.5}$	0.01	1.39	0.87	7.85	5.24	2.96	7.22	1.93

Here, it can be approximated that the amplitudes of all the K_{Tr_i} are the same (equal to A),

$$K_{Tri} = A \cos(2\pi f_S t - \varphi_i). \tag{7}$$

The force of the whole rotor, K_{Tr}, is

$$K_{Tr} = \sum_{i=1}^{n_r} K_{Tri} = \sum_{i=1}^{n_r} A \cos(2\pi f_S t - \varphi_i), \tag{8}$$

$$K_{Tr} = A \left[\sin(2\pi f_S t) \sum_{i=1}^{n_r} \sin(\varphi_i) + \cos(2\pi f_S t) \sum_{i=1}^{n_r} \cos(\varphi_i) \right]. \tag{9}$$

Define variables as follows:

$$a = \sum_{i=1}^{n_r} \sin(\varphi_i); \quad b = \sum_{i=1}^{n_r} \cos(\varphi_i). \tag{10}$$

K_{Tr} is

$$K_{Tr} = A\sqrt{a^2 + b^2} \sin(2\pi f_S t + \varphi_{all}), \tag{11}$$

where the φ_{all} is the phase angle of the total force of the rotor.

Then, the signal superposition coefficient, A^*, can be defined as

$$A^* = \sqrt{a^2 + b^2} \tag{12}$$

and K_{Tr} is

$$K_{Tr} = AA^* \sin(2\pi f_S t + \varphi_{all}). \tag{13}$$

The signal superposition results of the first several orders of f_S of K_{Tr_i} are shown in Table V.

For the PJP 6-4, as shown in Fig. 6(a), the signal of four rotor blades K_{Tr_i} can be divided into two groups (K_{Tr_1} and K_{Tr_3}; K_{Tr_2} and K_{Tr_4}). The phase difference between the adjacent groups is about 180° (at $k_2 = 1$, $\varphi_1 - \varphi_2 = 153° + 27° = 180°$). Then, at $k_2 = 2$, the four φ_i gradually approaching the same value with $\varphi = -163°$, leading to a signal superposition coefficient of $A^* = 4.00$.

Similarly, for the PJP 8-6, at $k_2 = 3$, the six φ_i gradually approaching the same value with $\varphi \approx -140°$, leading to a signal superposition coefficient of $A^* = 6.00$. As the number of rotor blades increases, this uniform phase is gradually destroyed by small irregular fluctuations, such as the PJP 10-8 (the eight φ_i is about 75°–92°, leading to a slight error between $A^* = 7.95$ and $n_r = 8$).

In general, it can be concluded that, for a pre-swirl PJP with an even number of rotor blades (n_r), the signal superposition-enhancement phenomenon of K_{Tr_i} will happen at the k_2-order

TABLE V. The superposition of the unsteady forces of rotor blades.

Model	Order	Phase angle	$i = 1$	$i = 2$	$i = 3$	$i = 4$	$i = 5$	$i = 6$	$i = 7$	$i = 8$	A^*
PJP 6-4	$k_2 = 1$	φ_i	153	−27	153	−28	$\cdots$	$\cdots$	$\cdots$	$\cdots$	0.03
	$k_2 = 2$		−163	−165	−163	−165	$\cdots$	$\cdots$	$\cdots$	$\cdots$	4.00
PJP 8-6	$k_2 = 1$	φ_i	−158	80	−38	−158	79	−38	$\cdots$	$\cdots$	0.11
	$k_2 = 2$		110	−129	−5	112	−132	−3	$\cdots$	$\cdots$	0.21
	$k_2 = 3$		−139	−142	−140	−144	−144	−142	$\cdots$	$\cdots$	6.00
PJP 10-8	$k_2 = 1$	φ_i	55	−33	−126	148	55	−31	−125	148	0.01
	$k_2 = 2$		−137	56	−132	69	−134	65	−127	61	1.04
	$k_2 = 3$		66	164	−99	−14	74	166	−101	−22	0.37
	$k_2 = 4$		79	84	75	92	79	92	76	90	7.95

dominant frequency ($k_2 f_S$, $k_2 = 1/2n_r$). The dominant frequency of the unsteady force of the whole rotor, K_{Tr}, will be moved from the stator blades passing frequency (for a single rotor blade), f_S, to its harmonic $k_2 f_S$. In addition, the signal superposition coefficient at $f = k_2 f_S$ will be $A^* = n_r$.

However, for the PJP with odd number of blades, at $J = 1.0$, the unsteady force of each rotor blade of the PJP 7-5, the PJP 9-7, and the PJP 11-9 is shown in Figs. 8(a)–8(c), respectively. The results show that no such obvious signal superposition-enhancement phenomenon is found for those three PJPs. As shown in Fig. 8(c), the peaks at nf_S of K_{Tr} are similar to that of K_{Tr_1}.

Hence, only the n_r is an even number, the signal superposition-enhancement phenomenon of unsteady force of rotor blades will happen at the k_2-order dominant frequency ($k_2 = 1/2n_r$).

Similarly, the forces of individual stator blades, K_{Ts_i}, are shown in Figs. 9(a) and 9(b). Based on the FFT results [see Figs. 9(c) and 9(d)], the characteristic frequency of K_{Ts_i} for both PJPs is nf_{BPF} (120, 240, 360, 480 Hz... for the PJP 8-6; 140, 280, 420, 560 Hz... for the PJP 9-7). In addition, for both PJPs, a peak at 650 Hz was observed. We guess this frequency is the shedding frequency of the stator trailing vortex, which will be discussed later. Here, although the number of stator blades is different, the incoming flow velocities of both PJPs are the same, resulting in the same vortex shedding period.

Furthermore, the comparison of different numbers of stator blade forces is shown in Fig. 10. First, the dominant frequency of a single stator blade is $1f_{BPF}$, that is, the passing frequency of the rotor blade.

With the increase in the number of stator blades (n_s), the amplitude of PSD decreases gradually.

For even n_s stators, as shown in Fig. 10(a) (the PJP 6-4), it can be seen that the peak at $1f_{BPF}$ and $2f_{BPF}$ decreases, while the peak value at $3f_{BPF}$ increases significantly. Similarly, the dominant frequency of K_{Ts_i} of the PJP 8-6 is $4f_{BPF}$ [see Fig. 10(c)], while that of 10-8 is $5f_{BPF}$ [see Fig. 10(e)]. In addition, for odd n_s stators [see Figs. 10(b), 10(d), and 10(f)], there is no signal superposition enhancement phenomenon as discussed before, but the increase in broadband component.

Therefore, the same conclusion holds for the stator: for a pre-swirl PJP with an even number of stator blades (n_s), the signal superposition-enhancement phenomenon will happen at the k_1-order dominant frequency ($k_1 = 1/2n_s$). The dominant frequency of the unsteady force of the stator, K_{Ts}, will be moved from the rotor blades passing frequency, f_{BPF}, to its harmonic $k_1 f_{BPF}$, $k_1 = 1/2n_s$. Combined with the conclusion of the rotor, it can be inferred that for a pre-swirl PJP with even blades (rotor or stator), the signal superposition-enhancement phenomenon will happen at the k-order dominant frequency ($k = 1/2n$, n is the corresponding blades number). As for the signal superposition enhancement coefficient of the stator, for the PJP 6-4, the PSD of K_{Ts_i} is 1.28×10^{-10}, the PSD of K_{Ts} is 5.48×10^{-9}, and the 0.5 square of the amplitude ratio is 6.54 (is close to $n_s = 6$); for the 8-6, the 0.5 square of the amplitude ratio is 12.60 (bigger than $n_s = 8$); for the PJP 10-8, it is 3.00 (smaller than $n_s = 10$). Therefore, for the stator blades, it is difficult to maintain
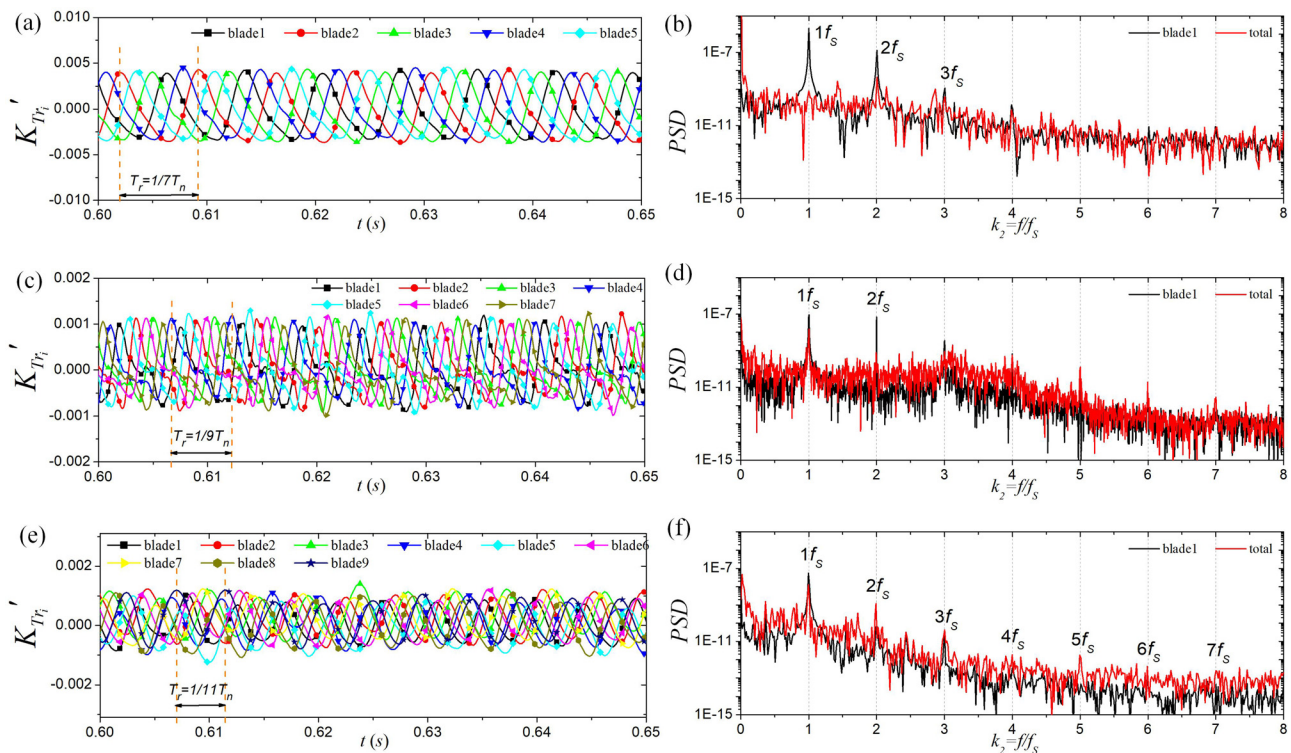

FIG. 8. The unsteady force of rotor blades in the case $J = 1.0$: (a) time history of the PJP 7-5; (b) PSD of the PJP 7-5; (c) time history of the PJP 9-7; (d) PSD of the PJP 9-7; (e) time history of the PJP 11-9; and (f) PSD of the PJP 11-9.
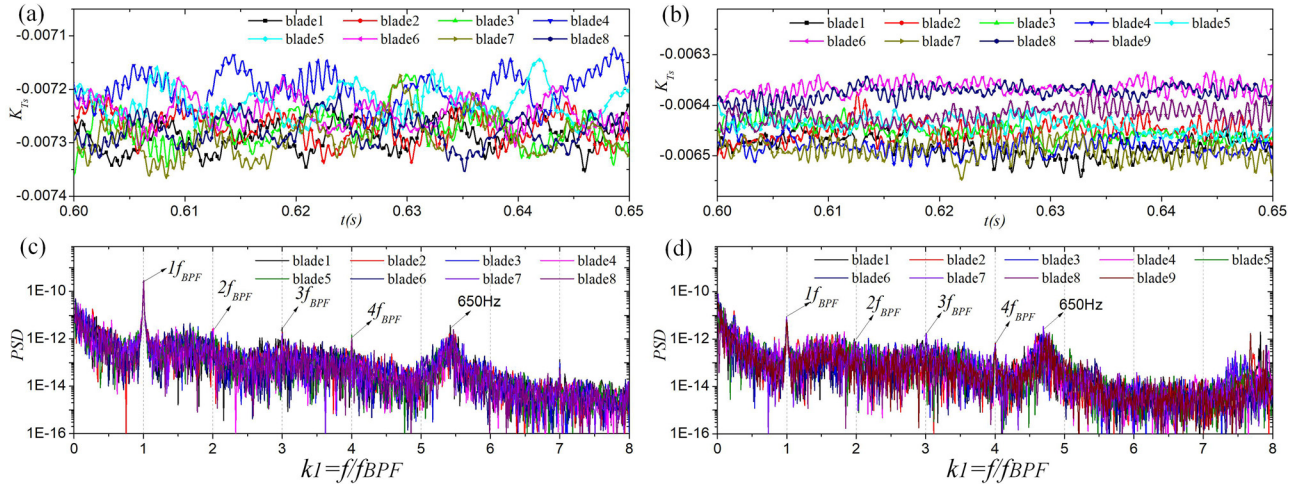
FIG. 9. Unsteady forces of stator blades for the PJP model in the case $J = 1.0$: (a) the time history of the PJP 8-6; (b) the time history of the PJP 9-7; (c) PSD of the PJP 8-6; and (d) PSD of the PJP 9-7.

$A^* = n_s$. The reason can be found from Fig. 9, and the mean value of K_{Ts_i} no longer remains a same value. In addition, the fluctuation amplitude of the stator blades is much smaller than that of the rotor blades.

More importantly, it is worth noting that the $k_1 f_B PF$ and $k_2 f_S$ is equal. It is well known that two objects vibrating at the same

frequency will resonate. For a PJP with an even rotor number n_r and an even stator number n_s, the dominant frequency of the unsteady force of the rotor will be $k f_S = 1/2 n_r f_S = 1/2 n_r n_s f_n$ and the dominant frequency of unsteady force of stator will be $k f_{BPF} = 1/2 n_s f_{BPF} = 1/2 n_s n_r f_n$. Therefore, for PJP with even numbers of
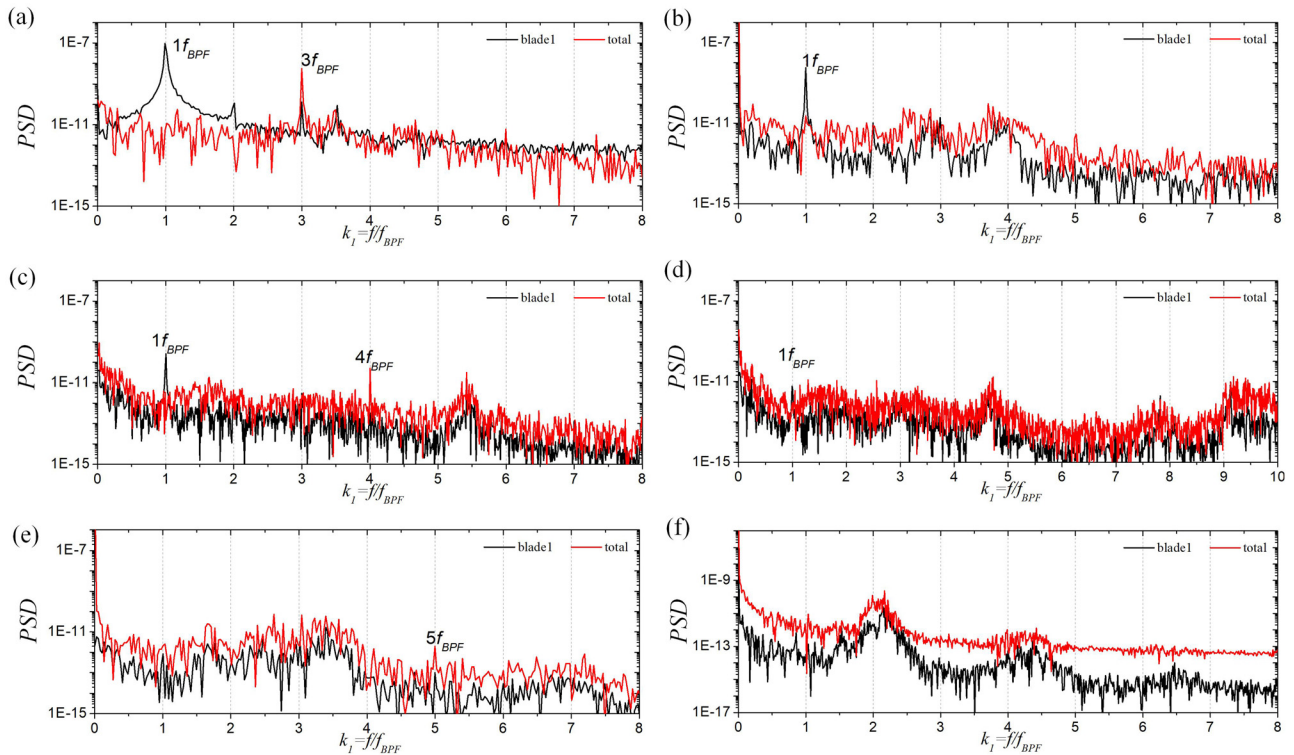

FIG. 10. Comparison of the PSD of the unsteady force between the single stator blade and the total stator: (a) the PJP 6-4; (b) the PJP 7-5; (c) the PJP 8-6; (d) the PJP 9-7; (e) the PJP 10-8; and (f) the PJP 11-9.

n_r and n_s, the rotor–stator resonance phenomenon occurs at $f = 1/2n_s n_r f_n$.

However, this does not mean that an even number of rotor blades cannot be used for PJP. As shown in Fig. 7, the dominant frequency of unsteady force of the rotor is transferred from $1f_S$ to $1/2n_r f_S$. Hence, this signal superposition weakening phenomenon at low frequency is valuable to transfer the dominant frequency from low frequency to high frequency. In addition, as shown in Table IV, the A^* at $k_2 = 1$ for the PJP 6-4 is 0.04; the A^* at $k_2 = 1$ for the PJP 8-6 is 0.23, and for PJP 10-8, it is 0.01, which means the even number of rotor blades will lead to a significant reduction of the pulsation amplitude of the force generated by the rotor at lower orders of dominant frequency, which will help to reduce the vibration and noise levels caused by the rotor.

B. Vortex structure and evolution

Next, take the PJP 8-6 and PJP 9-7 models as examples for comparison. Figures 11 and 12 show the instantaneous Q surfaces of the PJP 8-6 and the PJP 9-7 in the case of $J = 1.0$.

For both PJPs, a relative complex vortex system, which consists of the tip vortices, the hub vortices, the duct-induced vortex (see Fig. 11), the rotor trailing vortices, and the stator trailing vortices, is found for the PJP.

First, let us discuss the evolution of tip vortices. As shown in Fig. 11(a), obvious tip vortices can be found in the wake of PJP, which maintains a long distance downstream the duct. Furthermore, it should be noted that the spiral tip vortex filaments present a small amplitude oscillation in the form of a sinusoidal curve, which is very different from the standard spiral filament.[16] In the study of Qin et al.,[2] this form of oscillation is called short-wave instability of PJP,

caused by the stator blades. Qin et al.[2] compared the vortex structure of a normal PJP with the PJP without stator (contains rotor and duct), and it is found that the tip vortex of PJP presents a standard spiral shape without stator, which confirms the conclusion. This short-wave instability originates from the definition of Saffman,[28] in which the smooth-sinuous-wave-type mode of tip filaments is called as short-wave instability mode.

Besides the spiral tip filaments, it is clearly observed from Fig. 11 that some small vortices appear between the tip vortices, which evenly surround those spiral filaments. The structural form of those small vortices is the same as the "secondary vortex structure" according to Gong's research.[17] In his paper, those secondary vortices happen in the case of the ducted propeller, while no such vortices are generated for the same propeller without duct. Hence, those secondary vortices are caused by the duct.

The specific structure of the secondary vortices can be seen in Figs. 13(a) and 13(b). At the outer surface of the duct, a uniform layer of sheet vortex representing the boundary layer flow is found. With the fluid develops downstream, this sheet vortex gradually begins to separate from the wall, forming the duct-induced vortex with ring shapes as shown in Fig. 11(a). At the trailing edge of the duct, the duct-induced vortex begins to interact with the tip vortex, forming some broken small vortex groups rotating around the tip vortex, which is the reason for the generation of the secondary vortex.

More details of the secondary vortex can be seen in Fig. 14(c), in which the contour of x component of vorticity in the y–z plane is given. As shown in Fig. 14(d), the tip vortices can be obviously identified as a series of blue circles. However, a circle of small vortex is found around every tip vortex, whose upper part is red and the lower part is
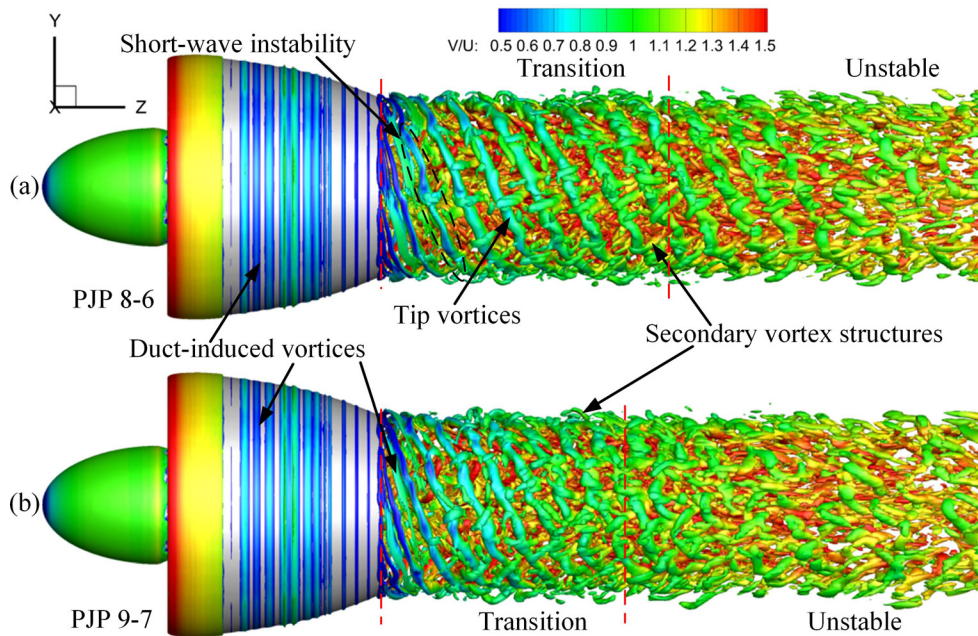

FIG. 11. Instantaneous Q surfaces ($Q = 10\,000$ s^{-2}) of the PJP in the case $J = 1.0$, colored by the velocity magnitude scaled by U: (a) the PJP 8-6 and (b) the PJP 9-7.

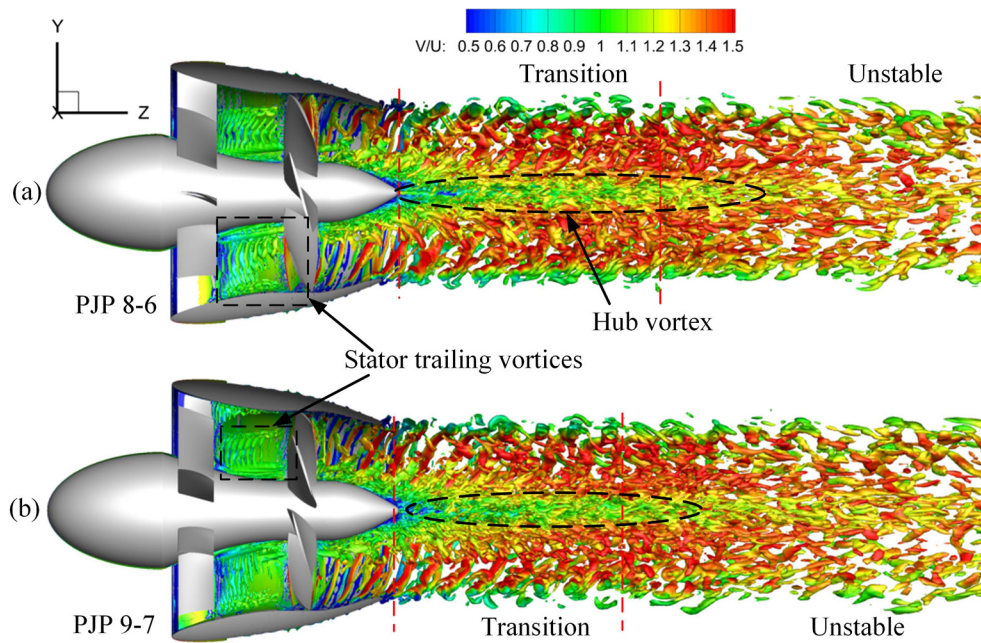**FIG. 12.** Half section view of the instantaneous Q surfaces ($Q = 10\,000$ s^{-2}) of the PJP, colored by the velocity magnitude scaled by U: (a) the PJP 8-6 and (b) the PJP 9-7.
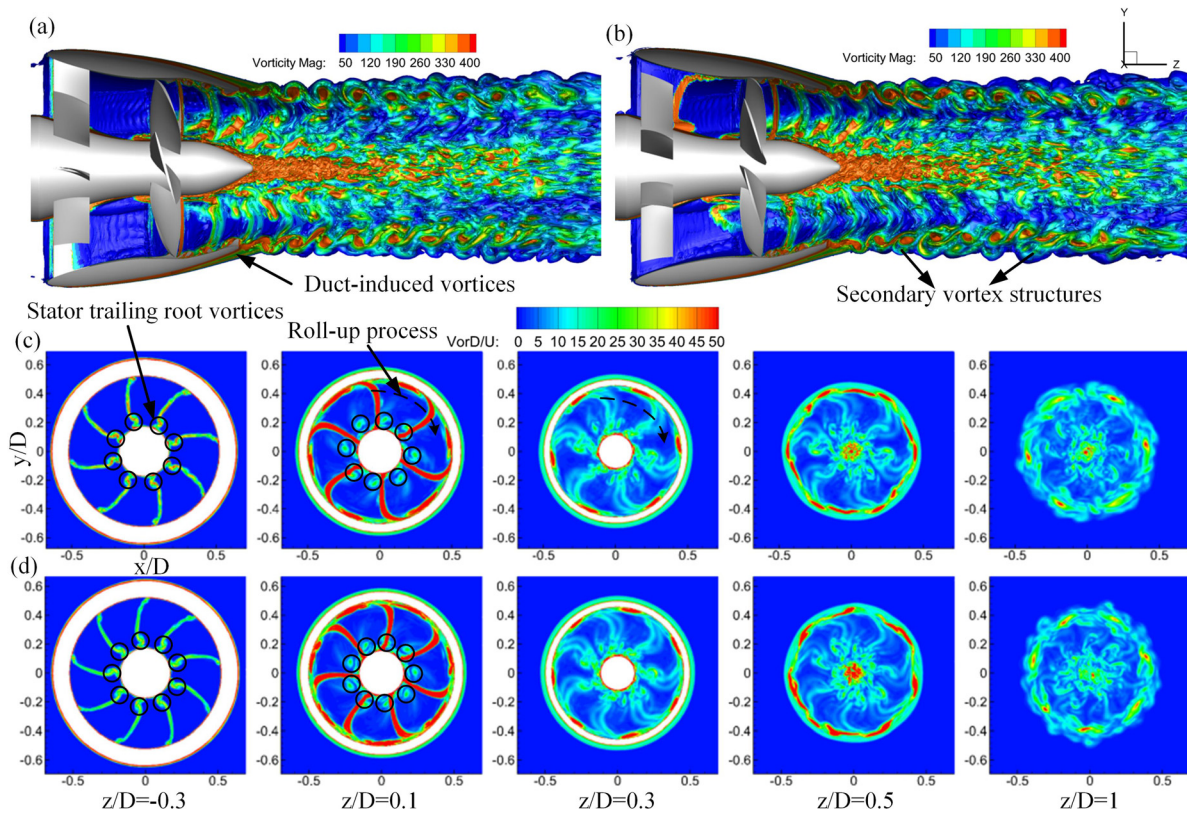

FIG. 13. Views of the vortices of PJP: (a) the instantaneous surfaces of vorticity magnitude of the PJP 8-6; (b) the instantaneous surfaces of vorticity magnitude of the PJP 9-7; (c) the vorticity magnitude in the x–y plane normalized with U/D of the PJP 8-6; and (d) the vorticity magnitude in the x–y plane normalized with U/D of the PJP 9-7.
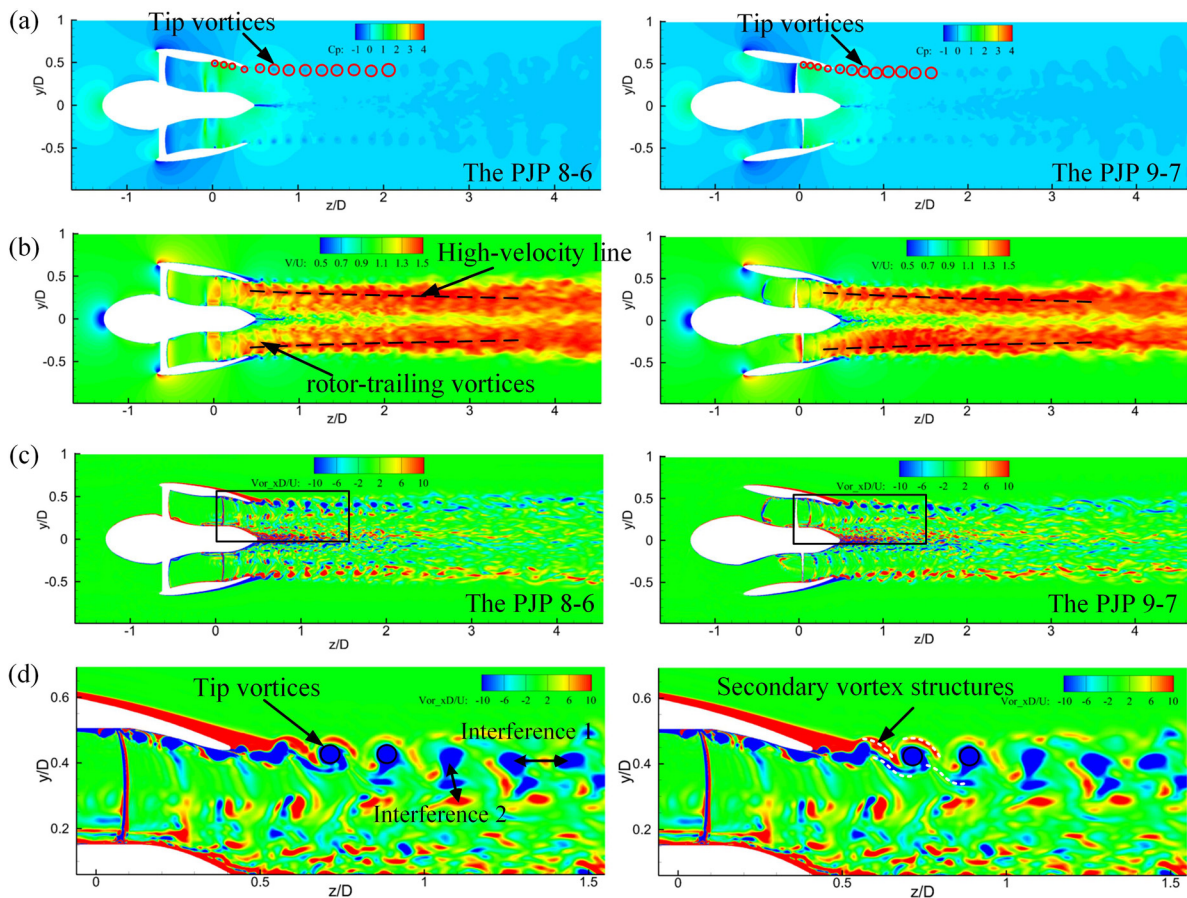
FIG. 14. Instantaneous flow field in the y–z plane: (a) the pressure coefficient; (b) the velocity magnitude; (c) the x component of vorticity normalized with U/D of $\alpha = 0°$; and (d) the zoom-in view.

blue. The secondary vortex (marked by white lines), which rotates around the tip vortices, is generated.

The secondary vortex, rotating around the tip filaments, will inevitably exert a force on the tip filaments, increasing the self-induction instability of tip vortices and changing the vortex tube from standard cylindrical to twist shape. As shown in Fig. 11, with the fluid flowing further downstream, there are more and more secondary vortices, accompanied by the increase in the twist degree of the spiral filaments of tip vortices.

According to Felli et al.,[16] the instability inception point of tip vortices is defined as the first position at which the gradient of the tip vortex envelope equals 50% of the maximum slope. Based on the location of the instability inception point, the wake of PJP can be divided into two parts: the transition region and the unstable region. The position of instability transition point has been marked with a dotted line as shown in Fig. 11. As shown, the transition-to-instability position of the PJP 9-7 (about $z/D = 1.6$) moves upstream with respect to the PJP 8-6 (about $z/D = 1.8$).

A clearer contrast of the tip vortices of the two PJPs is shown in Fig. 15. For the PJP 8-6, the tip filaments maintain a spiral for a long distance downstream of the duct. With fluid developing downstream,

the gradual twist of tip filaments happens until finally breaking down in the far field. However, for the PJP 9-7, the local wave amplitude of tip filament is much larger. A pairing phenomenon of adjacent tip filaments happens before the transition-to-instability position [see Fig. 15(b)].

The instantaneous positions of the tip vortices in the upper part of the y–z plane of PJPs are compared in Fig. 15(c). In the figure, the range of the duct region, the transition region, and the unstable region of PJPs are marked with blocks of different colors. The transition-to-instability position of the PJP 9-7 is at about $z/D = 1.6$, where the radius of tip vortices of the PJP 9-7 encounter small fluctuations due to the pairing phenomenon of tip filaments.

For both PJPs, the morphology of the tip vortices is gradually modified by the generation and growth of perturbations caused by the secondary vortices and adjacent tip filaments, which trigger the instability of tip vortices.

Furthermore, the axial distance between two adjacent helical filaments ($z_{i+1} - z_i$) is defined as the helical pitch of ith tip filament, P. As compared in Fig. 15(d), the P/D_{mean} of the PJP 9-7 is about 0.16, which is obviously smaller than that of PJP 8-6 with $P/D_{mean} = 0.2$. The reduction of the spiral-to-spiral distance of tip vortices can also be
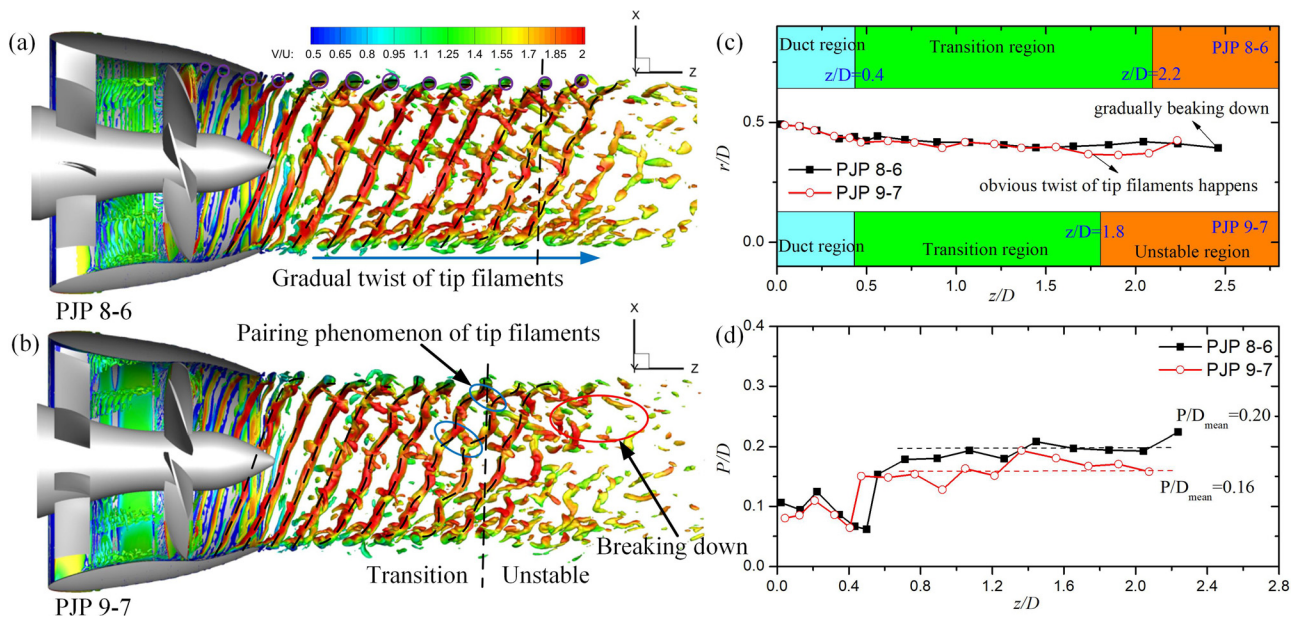
FIG. 15. View of the tip vortex structure of PJP ($Q = 50\,000$ s^{-2}): (a) the PJP 8-6; (b) the PJP 9-7; (c) the radius of the tip vortices core in the y–z plane; and (d) the helical pitch ratio.

observed in Fig. 14(a), where the uniform low-pressure regions (marked with red circles) caused by the tip vortex of the two PJPs show a clear difference. Hence, it looks like that the moving upstream of the transition-to-instability position for the PJP 9-7 is caused by the reduction of P/D.

This conjecture is consistent with the conclusion of Felli *et al.*[16] that the transition to the instability shows a clear dependence on the spiral-to-spiral distance. More specifically, the smaller the P/D is, the bigger is the mutual interaction between adjacent tip filaments, which means the tip filaments are more likely tending to interact mutually and form the pairing phenomenon. Hence, the transition-to-instability position moves upstream more and more with an increasing number of rotor blades (n_r), owing to the reduction of spiral-to-spiral distance. This supports the thesis of Felli *et al.*[16] that the instability triggering mechanism is the mutual interaction between adjacent tip spirals.

Second, we discuss the trailing edge vortices of PJPs. The stator trailing vortex, rotor trailing vortex, and hub vortex form the complex vortex system of PJP. There is a complex interaction between the three vortices.

As shown in Fig. 12, the stator trailing edge vortex is a layer of vortex falling off from the stator trailing edge. As shown in Fig. 13(c), eight trailing wakes of stator can be seen at $z/D = -0.3$, while nine for the PJP 9-7 [see Fig. 13(d)]. At $z/D = 0.1$, the upper part of stator trailing wakes has been dispersed, while only the root vortex (marked with black circles) is retained. Further downstream, those root vortices gradually interact with the rotor trailing wake, leading to the twist at the root of rotor trailing wake at $z/D = 0.3$. In general, with the development of fluid downstream, most of the stator trailing vortices break down due to viscous dissipation, while the stator trailing root vortex directly flows into the rotor domain and interacts with the rotor trailing vortex.

The spatial evolution process of rotor trailing wake [see Figs. 13(c) and 13(d)] is usually called the roll-up process (the upper part of the trailing edge vortex undergoes a progressively increasing angular displacement and a radial rise[2]).

The roll-up process of the rotor trailing vortex is caused by the velocity difference in the radius direction in the wake of propeller. As shown in Fig. 14(b), the convection speed of the upper part of trailing edge is larger than the root region [as shown by the high-velocity line in Fig. 14(b)], which will lead to a faster movement downstream.

As shown in Fig. 14(d), with the fluid developing downstream, the upper part of rotor trailing edge vortices gradually approach the tip vortices and will interfere with the adjacent tip vortex. This interference between trailing edge vortices and tip vortex is marked with "interference 2" in the figure, while the multi-interference between two adjacent tip vortices is marked with "interference 1."

According to the research of Wang *et al.*,[18] the two underlying mechanisms that trigger tip vortex instability is the interference between the trailing edge vortex and the tip vortex and multi-
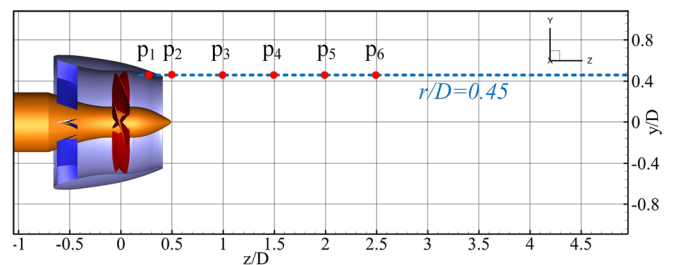

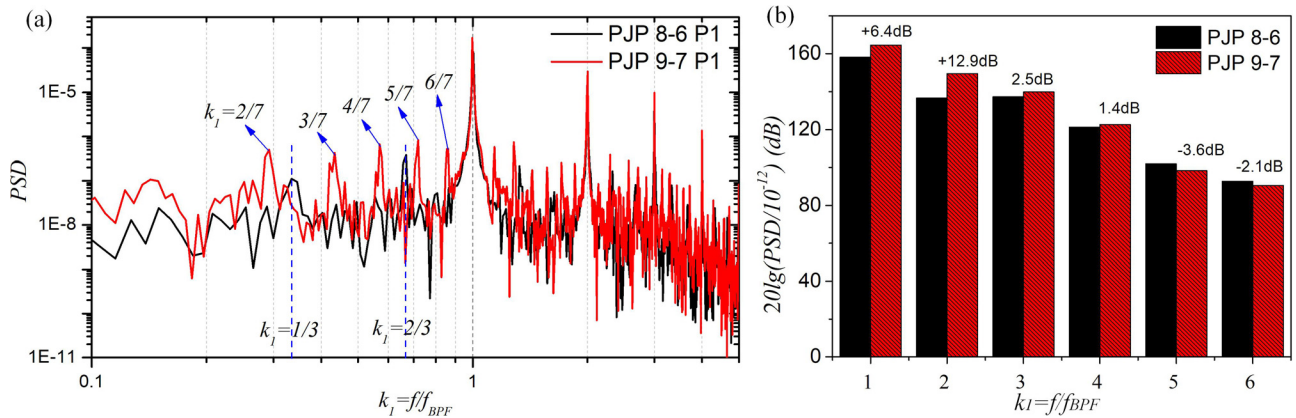
FIG. 16. Probes setting for the PJP.

FIG. 17. Comparison of TKE at P1 of the two PJPs: (a) the PSD and (b) the dimensionless quantity of PSD at kf_{BPF}.

inductance of tip vortices. As shown in Fig. 14(d), it looks like that, for both PJPs, the roll-up process and the contact process between the trailing edge vortex and the tip vortex is the same. According to the research of Okulov,[29] the instability of rotor tip vortices is considered triggered by the complete development of the roll-up process. This seems to be in contrast with the results here that the transition-to-instability position of PJP 9-7 moves upstream than the PJP 8-6. We speculate that the interference between trailing edge vortices and tip vortex is small. For PJP, the instability of tip vortex is more triggered by multi-inductance of tip vortices. This is consistent with the conclusion of Felli *et al.* that the transition to instability is correlated more to the mutual interference between consecutive vortices than to the complete development of the roll-up process of the rotor trailing wake.[16]

In general, for PJP, the instability of the tip vortex show a clear dependence on the number of rotors (not depending on the parity of the number of rotors). The greater the number of rotor blades is, the shorter the spiral-to-spiral distance is, and the greater the mutual inductance between tip vortices is, which triggers the instability of tip vortices. The transition-to-insatiability point of the rotor tip vortex moves upstream with an increasing number of rotor blades.

Furthermore, the evolution of the wake flow can be inspected by analyzing the kinetic energy $K = 0.5(u^2 + v^2 + w^2)$. To this end, six probes (probes P1,…, P6) are created ($r/D = 0.45$, $z/D = 0.2, 0.5, 1, 1.5, 2, 2.5$) as shown in Fig. 16.

The power spectral density (PSD) of the turbulence kinetic energy (TKE) at probes P1 is shown in Fig. 17. For both PJPs, the obvious peaks at nf_{BPF} can be found in the power spectrum, which is consistent with the conclusion of Mascio *et al.*[30] that the TKE spectra in the tip region of E779A are characterized by peaks of nf_{BPF}. The dimensionless PSD values at nf_{BPF} using $20lg\left(PSD/(1 \times 10^{-12})\right)$ (dB) are shown in Fig. 17(b). At $k_1 = 1$, the PSD of P1 for the PJP 9-7 is 6.4 dB bigger than the PJP 8-6, and it is 12.9 and 2.5 dB at $k_1 = 2$ and $k_1 = 3$. Hence, similar to the unsteady force generated by the rotor, the fluctuation amplitude of TKE at the tip of the PJP 9-7 is bigger than the PJP 8-6 at low-frequency range.

In addition, several peaks at $k_1 = 1/3$ and $k_1 = 2/3$ are found for the PJP 8-6, while $k_1 = 2/7$, $k_1 = 3/7$, …, $k_1 = 6/7$ are found for the PJP 9-7. Those frequency is the shaft frequency and its harmonics. For the PJP 8-6, it looks like that only the peak at $f_i = 2if_n$, $i = 1, 2, 3, …$ due to the even number of rotor blades. For the PJP 9-7
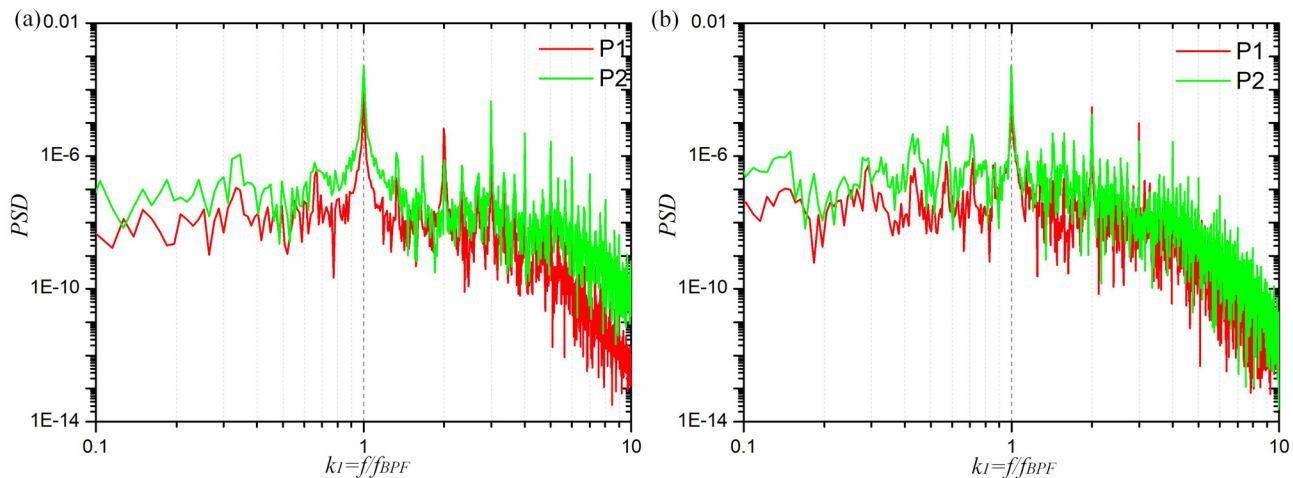

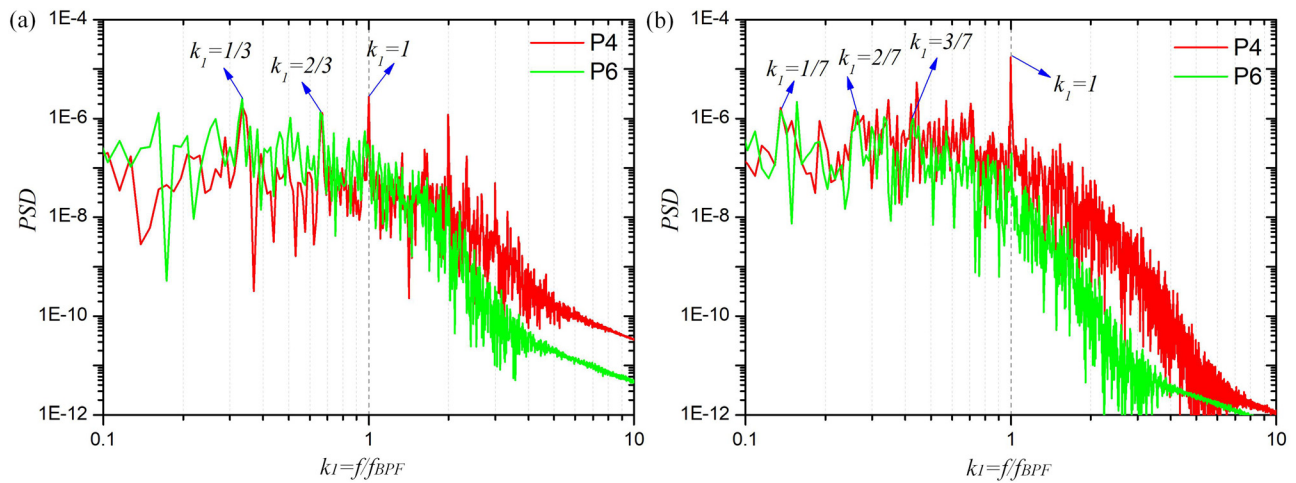**FIG. 18.** PSD of TKE at P1 and P2: (a) the PJP 8-6 and (b) the PJP 9-7.

FIG. 19. PSD of TKE at P4, P6: (a) the PJP 8-6 and (b) the PJP 9-7.

with an odd number of rotor blades, it happens at $f_i = i f_N$, $i = 1, 2, 3,$ .... Therefore, the odd and even number of rotor blades will result in a different line spectrum of TKE at the tip region.

Furthermore, Fig. 18 shows the distribution of the normalized power spectrum of P1 and P2 of PJPs. The amplitude of power spectrum of P2 increases obviously with respect to P1 for both PJPs. As discussed before, at P2 ($z/D = 0.5$, right behind the duct), the secondary vortices are generated due to the duct, and the tip filaments of both PJPs are disturbed by interactions induced by those secondary vortices. This is why the power spectrum of P2 has a bigger amplitude.

As proposed by Felli *et al.*,[16] for a single propeller, the energy transfer from blade harmonics to shaft harmonics will happen in the wake field. Here, similarly, from the transition region (P4) to the unstable region (P6), the peak at $n f_{BPF}$ reduces obviously for both PJPs (see Fig. 19). At P6, the shaft harmonics is the main contribution of the spectrum for both PJPs. Therefore, the energy transfer process from blade harmonics to shaft harmonics of the pre-swirl PJP is similar with the single propeller.

V. CONCLUSIONS

In this paper, DES simulations are carried out to investigate the effect of an odd and even number of rotor/stator blades on the hydrodynamic performance of the pre-swirl pumpjet propulsor (PJP). The hydrodynamic performance, the unsteady force of blades, and the vortex structure of six PJPs, the PJP 6-4 (n_s–n_r), 8-6, 10-8, 7-5, 9-7, and 11-9, are compared.

The study aims to get insight into the relationships between the hydrodynamic performance of the PJP and the parity of rotor/stator blades as well as to highlight the main features of the vortex destabilizing mechanisms for the PJP.

The results show that for the pre-swirl PJP, the characteristic frequency of the unsteady force of a single rotor blade is the stator blade passing frequency and its harmonics, which does not depend on the number of the blade. In contrast, the characteristic frequency of unsteady force of the whole rotor depends on the number or, more accurately, on the parity of the number of rotor blade:

(1) For a pre-swirl PJP with an even number of n_r, the signal superposition-enhancement phenomenon of unsteady forces of rotor blades will happen at the k-order dominant frequency ($k = 1/2n_r$). More importantly, the signal superposition coefficient at $k = 1/2n_r$ is $A^* = n_r$, at least from the present tests. The dominant frequency of the unsteady force of the rotor will be moved from the stator blades passing frequency, f_S, to its harmonic $k f_S$, $k = 1/2n_r$.

(2) For a pre-swirl PJP with an odd number of rotor blades (n_r), the amplitude of K_{Tr} changes slightly with respect to a single rotor blade. The dominant frequency of the unsteady force of the rotor, K_{Tr}, is still the stator blades passing frequency, f_S.

In terms of both the rotor and stator numbers are even, a phenomenon of the rotor–stator resonance occurs at $f = 1/2n_s n_r f_n$, where f_n represents the hub rotational frequency.

In addition, the instability of tip vortex of the PJP depends on the number of rotor blades (the spiral-to-spiral distance). The greater the number of rotor blades, the shorter the spiral-to-spiral distance, and the faster the instability of tip vortices happens. The transition-to-insatiability point of the rotor tip vortex moves upstream with an increasing number of rotor blades, and it is independent of the number of stators.

AUTHOR DECLARATIONS
Conflict of Interest

The authors declare that they have no conflicts of interest associated with this work.

DATA AVAILABILITY

The data that support the findings of this study are available within the article and are available from the corresponding author upon reasonable request.

REFERENCES

[1] D. Qin, Q. Huang, Y. Shi, G. Pan, Y. Shi, and X. Dong, "Comparison of hydrodynamic performance and wake vortices of two typical types of pumpjet propulsor," Ocean Eng. **224**, 108700 (2021).

[2] D. Qin, Q. Huang, G. Pan, Y. Shi, P. Han, and X. Dong, "Effect of the duct and the pre-swirl stator on the wake dynamics of a pre-swirl pumpjet propulsor," Ocean Eng. **237**, 109620 (2021).

[3] B. McCormick and J. Elsenhuth, "Design and performance of propellers and pumpjets for underwater propulsion," AIAA J. **1**, 2348–2354 (1963).

[4] M. J. Hughes and S. A. Kinnas, "An analysis method for a ducted propeller with pre-swirl stator blades," in Proceedings of the Propellers/Shafting '91 Symposium, No. 15, SNAME, Virginia Beach, VA (1991), available at https://trid.trb.org/view/440900.

[5] C. Suryanarayana, B. Satyanarayana, K. Ramji, and A. Saiju, "Experimental evaluation of pumpjet propulsor for an axisymmetric body in wind tunnel," Int. J. Naval Archit. Ocean Eng. **2**, 24–33 (2010).

[6] C. Suryanarayana, B. Satyanarayana, K. Ramji, and M. N. Rao, "Cavitation studies on axi-symmetric underwater body with pumpjet propulsor in cavitation tunnel," Int. J. Naval Archit. Ocean Eng. **2**, 185–194 (2010).

[7] C. Suryanarayana, B. Satyanarayana, and K. Ramji, "Performance evaluation of an underwater body and pumpjet by model testing in cavitation tunnel," Int. J. Naval Archit. Ocean Eng. **2**, 57–67 (2010).

[8] H. Das, P. Jayakumar, V. Saji, R. Yerram et al., "CFD examination of interaction of flow on high-speed submerged body with pumpjet propulsor," in 5th International Conference on High Performance Marine Vehicles, Launceston, Australia (IEEE, 2006), pp. 466–479.

[9] L. Lu, G. Pan, and P. K. Sahoo, "CFD prediction and simulation of a pumpjet propulsor," Int. J. Naval Archit. Ocean Eng. **8**, 110–116 (2016).

[10] L. Lu, Y. Gao, Q. Li, and L. Du, "Numerical investigations of tip clearance flow characteristics of a pumpjet propulsor," Int. J. Naval Archit. Ocean Eng. **10**, 307 (2018).

[11] D. Qin, G. Pan, Q. Huang, Z. Zhang, and J. Ke, "Numerical investigation of different tip clearances effect on the hydrodynamic performance of pumpjet propulsor," Int. J. Comput. Methods **15**, 1850037 (2018).

[12] C. Qiu, Q. Huang, G. Pan, Y. Shi, and X. Dong, "Numerical simulation of hydrodynamic and cavitation performance of pumpjet propulsor with different tip clearances in oblique flow," Ocean Eng. **209**, 107285 (2020).

[13] Y. Sun, W. Liu, and T.-Y. Li, "Numerical investigation on noise reduction mechanism of serrated trailing edge installed on a pump-jet duct," Ocean Eng. **191**, 106489 (2019).

[14] D. Qin, Q. Huang, G. Pan, P. Han, Y. Luo, and X. Dong, "Numerical simulation of vortex instabilities in the wake of a preswirl pumpjet propulsor," Phys. Fluids **33**, 055119 (2021).

[15] H. Li, Q. Huang, G. Pan, and X. Dong, "Wake instabilities of a pre-swirl stator pump-jet propulsor," Phys. Fluids **33**, 085119 (2021).

[16] M. Felli, R. Camussi, and F. Di Felice, "Mechanisms of evolution of the propeller wake in the transition and far fields," J. Fluid Mech. **682**, 5 (2011).

[17] J. Gong, J. Ding, and L. Wang, "Propeller–duct interaction on the wake dynamics of a ducted propeller," Phys. Fluids **33**, 074102 (2021).

[18] L. Wang, T. Wu, J. Gong, and Y. Yang, "Numerical simulation of the wake instabilities of a propeller," Phys. Fluids **33**, 125125 (2021).

[19] L. Wang, T. Wu, J. Gong, and Y. Yang, "Numerical analysis of the wake dynamics of a propeller," Phys. Fluids **33**, 095120 (2021).

[20] L. Liu, M. Chen, J. Yu, Z. Zhang, and X. Wang, "Full-scale simulation of self-propulsion for a free-running submarine," Phys. Fluids **33**, 047103 (2021).

[21] W. Zhang, X. Ning, F. Li, H. Guo, and S. Sun, "Vibrations of simplified rudder induced by propeller wake," Phys. Fluids **33**, 083618 (2021).

[22] Y. Sanada, S. Park, D.-H. Kim, Z. Wang, F. Stern, and H. Yasukawa, "Experimental and computational study of hull–propeller–rudder interaction for steady turning circles," Phys. Fluids **33**, 127117 (2021).

[23] A. Posa and R. Broglia, "Flow over a hydrofoil at incidence immersed within the wake of a propeller," Phys. Fluids **33**, 125108 (2021).

[24] M. L. Shur, P. R. Spalart, M. K. Strelets, and A. K. Travin, "A hybrid RANS-LES approach with delayed-DES and wall-modelled LES capabilities," Int. J. Heat Fluid Flow **29**, 1638–1649 (2008).

[25] M. S. Gritskevich, A. V. Garbaruk, J. Schütze, and F. R. Menter, "Development of DDES and IDDES formulations for the k-ω shear stress transport model," Flow Turbul. Combust. **88**, 431–449 (2012).

[26] D. Qin, G. Pan, S. Lee, Q. Huang, and Y. Shi, "Underwater radiated noise reduction technology using sawtooth duct for pumpjet propulsor," Ocean Eng. **188**, 106228 (2019).

[27] I. B. Celik, U. Ghia, P. J. Roache, C. J. Freitas, H. Coleman, and P. E. Raad, "Procedure for estimation and reporting of uncertainty due to discretization in CFD applications," J. Fluids Eng. **130**, 078001 (2008).

[28] P. G. Saffman, "The velocity of viscous vortex rings," Stud. Appl. Math. **49**, 371–380 (1970).

[29] V. Okulov, "On the stability of multiple helical vortices," J. Fluid Mech. **521**, 319–342 (2004).

[30] A. D. Mascio, R. Muscari, and G. Dubbioso, "On the wake dynamics of a propeller operating in drift," J. Fluid Mech. **754**, 263–307 (2014).